

See discussions, stats, and author profiles for this publication at: <https://www.researchgate.net/publication/6328242>

# Calculations of and Evidence for Chain Packing Stress in Inverse Lyotropic Bicontinuous Cubic Phases

ARTICLE *in* LANGMUIR · JULY 2007

Impact Factor: 4.46 · DOI: 10.1021/la700355a · Source: PubMed

---

CITATIONS

35

---

READS

26

8 AUTHORS, INCLUDING:



**Charlotte E Conn**

The Commonwealth Scientific and Industrial ...

**41** PUBLICATIONS **738** CITATIONS

SEE PROFILE



**John M Seddon**

Imperial College London

**176** PUBLICATIONS **5,015** CITATIONS

SEE PROFILE



**Richard H Templer**

Imperial College London

**129** PUBLICATIONS **6,119** CITATIONS

SEE PROFILE

# Calculations of and Evidence for Chain Packing Stress in Inverse Lyotropic Bicontinuous Cubic Phases

Gemma C. Shearman,<sup>†</sup> Bee J. Khoo,<sup>†</sup> Mary-Lynn Motherwell,<sup>†</sup> Kenneth A. Brakke,<sup>‡</sup> Oscar Ces,<sup>†</sup> Charlotte E. Conn,<sup>†</sup> John M. Seddon,<sup>†</sup> and Richard H. Templer<sup>\*,†</sup>

Department of Chemistry, Imperial College London, SW7 2AZ United Kingdom, and Mathematics Department, Susquehanna University, Selinsgrove, Pennsylvania 17870

Received February 7, 2007. In Final Form: April 4, 2007

Inverse bicontinuous cubic lyotropic phases are a complex solution to the dilemma faced by all self-assembled water–amphiphile systems: how to satisfy the incompatible requirements for uniform interfacial curvature and uniform molecular packing. The solution reached in this case is for the water–amphiphile interfaces to deform hyperbolically onto triply periodic minimal surfaces. We have previously suggested that although the molecular packing in these structures is rather uniform the relative phase behavior of the gyroid, double diamond, and primitive inverse bicontinuous cubic phases can be understood in terms of subtle differences in *packing frustration*. In this work, we have calculated the packing frustration for these cubics under the constraint that their interfaces have constant mean curvature. We find that the relative packing stress does indeed differ between phases. The gyroid cubic has the least packing stress, and at low water volume fraction, the primitive cubic has the greatest packing stress. However, at very high water volume fraction, the double diamond cubic becomes the structure with the greatest packing stress. We have tested the model in two ways. For a system with a double diamond cubic phase in excess water, the addition of a hydrophobe may release packing frustration and preferentially stabilize the primitive cubic, since this has previously been shown to have lower curvature elastic energy. We have confirmed this prediction by adding the long chain alkane tricosane to 1-monoolein in excess water. The model also predicts that if one were able to hydrate the double diamond cubic to high water volume fractions, one should destabilize the phase with respect to the primitive cubic. We have found that such highly swollen metastable bicontinuous cubic phases can be formed within onion vesicles. Data from monoelaidin in excess water display a well-defined transition, with the primitive cubic appearing above a water volume fraction of 0.75. Both of these results lend support to the proposition that differences in the packing frustration between inverse bicontinuous cubic phases play a pivotal role in their relative phase stability.

## Introduction

When mixed with water, biologically relevant amphiphiles self-assemble to form a wide variety of lyotropic liquid crystalline structures. These include the fluid lamellar phase,  $L_\alpha$ ,<sup>1</sup> the inverse hexagonal phase,  $H_{II}$ ,<sup>2,3</sup> the inverse bicontinuous cubic phases,  $Q_{II}^P$ ,  $Q_{II}^D$ , and  $Q_{II}^G$ ,<sup>4</sup> and the inverse micellar cubic phases,  $Q_{II}^m$ .<sup>5</sup> All of these structures are based upon lipid monolayers, the basic building blocks of biological membranes. Of these, the most complex are the inverse bicontinuous cubic phases which consist of a pair of monolayers back-to-back (a bilayer) draped over the primitive (P), double diamond (D), and gyroid (G) triply periodic minimal surfaces (Figure 1). The inverse bicontinuous cubic phases have been the subject of significant research for more than two decades and have been found to occur in a wide variety of amphiphilic systems<sup>6–8</sup> as well as in block copolymer systems.<sup>9</sup> They are now believed to perform important biological func-

tions,<sup>10,11</sup> they have been observed in cells and organelles,<sup>12,13</sup> and the mechanism of their formation from the lamellar phase is a fundamental step in the mechanism of membrane fusion and fission.<sup>14,15</sup> The inverse bicontinuous cubic phases have also attracted considerable biotechnological interest in areas such as protein crystallization<sup>16,17</sup> and drug delivery.<sup>18</sup>

Despite significant advances, the energetic basis for the observed phase behavior of the inverse bicontinuous cubic phases is still poorly understood.<sup>19–24</sup> In particular, consideration of the competition between the incompatible demands for uniform, homogeneous interfacial curvature and uniform chain packing in lyotropic structures has not yet been applied to the inverse bicontinuous cubic phases.<sup>21,25</sup> In this model, the total free energy

\* To whom correspondence should be addressed. E-mail: r.templer@imperial.ac.uk.

<sup>†</sup> Imperial College London.

<sup>‡</sup> Susquehanna University.

- (1) McBain, J. W.; Marsden, S. S. *Acta Crystallogr.* **1948**, *1*, 270–272.
- (2) Luzzati, V.; Husson, F. *J. Cell Biol.* **1962**, *12*, 207–219.
- (3) Stoeckenius, W. *J. Cell Biol.* **1962**, *12*, 221–229.
- (4) Scriven, L. E. *Nature* **1976**, *263*, 123–125.
- (5) Seddon, J. M.; Robins, J.; Gulik-Krzywicki, T.; Delacroix, H. *Phys. Chem. Chem. Phys.* **2000**, *2*, 4485–4493.
- (6) Lindblom, G.; Larsson, K.; Johansson, L.; Fontell, K.; Forsen, S. *J. Am. Chem. Soc.* **1979**, *101*, 5465–5470.
- (7) Turner, D. C.; Wang, Z. G.; Gruner, S. M.; Mannock, D. A.; McElhaney, R. N. *J. Phys. II* **1992**, *2*, 2039–2063.
- (8) Templer, R. H.; Seddon, J. M.; Warrender, N. A.; Strykh, A.; Huang, Z.; Winter, R.; Erbes, J. *J. Phys. Chem. B* **1998**, *102*, 7251–7261.
- (9) Bates, F. S.; Fredrickson, G. H. *Phys. Today* **1999**, *52*, 32–38.

- (10) Seddon, J. M. *Biochim. Biophys. Acta* **1990**, *1031*, 1–69.
- (11) Burger, K. N. *J. Traffic* **2000**, *1*, 605–613.
- (12) Landt, T. *FEBS Lett.* **1995**, *369*, 13–17.
- (13) Almsheerqi, Z. A.; Kohlwein, S. D.; Deng, Y. *J. Cell Biol.* **2006**, *173*, 839–844.
- (14) Jahn, R.; Grubmuller, H. *Curr. Opin. Cell Biol.* **2002**, *14*, 488–495.
- (15) Kozlovsky, Y.; Kozlov, M. M. *Biophys. J.* **2003**, *85*, 85–96.
- (16) Caffrey, M. *J. Struct. Biol.* **2003**, *142*, 108–132.
- (17) Sennoga, C.; Heron, A.; Seddon, J. M.; Templer, R. H.; Hankamer, B. *Acta Crystallogr., Sect. A: Found. Crystallogr. D* **2003**, *59*, 239–246.
- (18) Drummond, C. J.; Fong, C. *Curr. Opin. Colloid Interface Sci.* **1999**, *4*, 449–456.
- (19) Helfrich, W.; Rennschuh, H. *J. Phys.* **1990**, *51*, C7189–C7195.
- (20) Templer, R. H.; Seddon, J. M.; Duesing, P. M.; Winter, R.; Erbes, J. *J. Phys. Chem. B* **1998**, *102*, 7262–7271.
- (21) Duesing, P. M.; Templer, R. H.; Seddon, J. M. *Langmuir* **1997**, *13*, 351–359.
- (22) Templer, R. H.; Turner, D. C.; Harper, P.; Seddon, J. M. *J. Phys. II* **1995**, *5*, 1053–1065.
- (23) Vacklin, M.; Khoo, B. J.; Madan, K. H.; Seddon, J. M.; Templer, R. H. *Langmuir* **2000**, *16*, 4741–4748.
- (24) Schwarz, U. S.; Gompper, G. *Phys. Rev. Lett.* **2000**, *85*, 1472–1475.

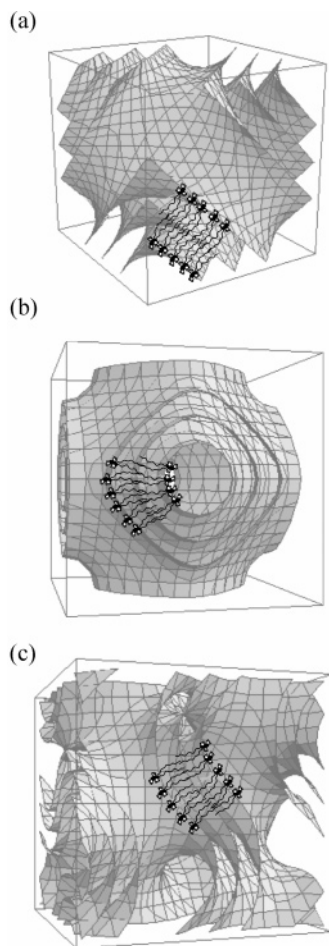


**Figure 1.** Unit cells for the three inverse bicontinuous cubic phases: (a) the  $Q_{II}^D$  phase with the space group  $Pn3m$ , (b) the  $Q_{II}^P$  phase with the space group  $Im3m$ , and (c) the  $Q_{II}^G$  phase, which belongs to space group  $Ia3d$ . The amphiphilic monolayers draped on either side of the underlying TPMS are indicated.

of a phase is taken to be the sum of the curvature elastic energy of the monolayer, the chain packing energy in the monolayer, and all the nonlocal interaction energies between the monolayers, such as the hydration repulsion energy between apposed polar interfaces. One may then simplify the model without apparently losing the essential features of relative phase behavior by only considering the curvature elastic and packing free energies.

No one has yet used this idea to explain the relative phase behavior of the inverse bicontinuous cubic phases, simply because the chain extension variance in inverse bicontinuous cubic phases of constant mean interfacial curvature has only been reported for the D cubic,  $Q_{II}^D$ .<sup>26</sup> We have therefore extended this work and calculated the variances in chain extension in  $Q_{II}^D$ ,  $Q_{II}^G$ , and  $Q_{II}^P$ . We report both our determinations of the dimensionless variance in chain extension for each structure and the distribution of the chain extension over the bicontinuous structures.

In the second half of the paper, we have experimentally tested the model. We have done this by combining our findings from previously reported calculations of the curvature elastic energy of inverse bicontinuous cubic phases of constant mean interfacial curvature<sup>20</sup> with the chain packing calculations reported here. Our curvature elastic calculations indicated that, in excess water,

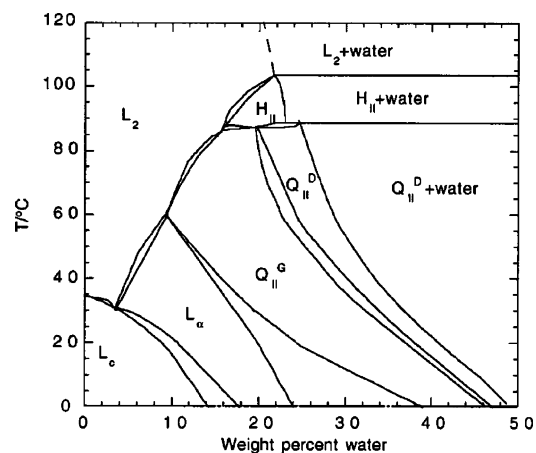


**Figure 2.** Phase diagram for 1-MO, drawn from the data of Briggs, Chung, and Caffrey.<sup>28</sup> The region designated by  $L_2$  is the inverse micellar solution phase, and the region designated by  $L_c$  is the lamellar crystal phase. All other phases are defined in the text.

the  $Q_{II}^P$  phase should have lower curvature elastic energy than the  $Q_{II}^D$  phase. Our calculations of the variance in chain extension indicate that, for water volume fractions usually observed in equilibrium measurements, the reverse is true for the chain packing energy. Therefore, this model predicts that by relieving the packing stress in the equilibrium, excess water  $Q_{II}^D$  phase we should be able to stabilize  $Q_{II}^P$ . We have experimentally tested this by adding long chain alkane to the monoacylglyceride 1-monoolein (1-MO) in water. Studied successively by Hyde and co-workers<sup>27</sup> and by Caffrey's group,<sup>28</sup> this system exhibits an extended region of  $Q_{II}^D$  in excess water but no  $Q_{II}^P$  phase (Figure 2). Our experiments show both that the free energy stored in the system due to the raised curvature elastic stress in  $Q_{II}^D$  will melt the long chain alkane and that once molten it enters the lyotropic mesophase and stabilizes the  $Q_{II}^P$  phase.

A surprising result of our calculations of packing stress is that, at very high water volume fractions well beyond the excess water point observed in equilibrium phases, the  $Q_{II}^P$  phase should become stabilized with respect to the  $Q_{II}^D$  phase. In recent experiments where we have recorded the out-of-equilibrium structural transformations that occur during the lamellar to bicontinuous cubic transition, we have observed very high water volume fraction structures. In particular, we have observed metastable, swollen bicontinuous cubic phases within the core of multilamellar (onion) vesicles and as intermediate phases during phase transitions of monoelaidin (ME) in water.<sup>29</sup> All of the data we have acquired indicates that there is a clear transition from  $Q_{II}^D$  to  $Q_{II}^P$  as water composition is increased, consistent with our model.

### Calculation of Variance in Chain Extension

**Background Concepts.** In the absence of any restraints on the curvature of an amphiphilic monolayer, a spherical interface will be formed unless the spontaneous curvature happens to be zero, which would be quite unusual for a monolayer.<sup>30</sup> In the case of type II amphiphiles (those amphiphiles that tend to form inverse phases), the interface bends toward the water and this interfacial geometry reflects the fact that the amphiphiles seek

(25) Kirk, G. L.; Gruner, S. M.; Stein, D. L. *Biochemistry* **1984**, *23*, 1093–1102.

(26) Anderson, D. M.; Gruner, S. M.; Leibler, S. *Proc. Natl. Acad. Sci. U.S.A.* **1988**, *85*, 5364–5368.

(27) Hyde, S. T.; Andersson, S.; Ericsson, B.; Larsson, K. Z. *Kristallogr.* **1984**, *168*, 213–219.

(28) Briggs, J.; Chung, H.; Caffrey, M. *J. Phys. II* **1996**, *6*, 723–751.

(29) Conn, C. E.; Ces, O.; Mulet, X.; Finet, S.; Winter, R.; Seddon, J. M.; Templer, R. H. *Phys. Rev. Lett.* **2006**, *96*.

(30) Templer, R. H.; Khoo, B. J.; Seddon, J. M. *Langmuir* **1998**, *14*, 7427–7434.

to achieve a time-averaged conical shape where the head group cross-sectional area is smaller than the cross-sectional area at the chain terminus. In other words, amphiphiles exert a two-dimensionally isotropic stress in the plane of the interface which, in the absence of other physical constraints, gives rise to a cylindrically symmetric molecular splay.

Sadoc and Charvolin<sup>31</sup> pointed out that where we have one amphiphilic species in water, it is impossible for inverse lyotropic phases to simultaneously have uniform interfacial curvature (let alone the preferred spherical interfacial geometry) and pack the hydrophobic core of the phase uniformly. The simplest case to illustrate this with is the inverse hexagonal phase (Figure 3). Simple calculations of the two-dimensional hexagonal packing of cylinders show that if the monolayer is to be cylindrical (such that every amphiphile has the same average shape), 9% of the hydrophobic interior of the phase will consist of empty “voids” around the hexagonal interstices. The energetic cost of such vacuum is too high to sustain, and the amphiphiles must alter their shape (nonuniformly around the cylinder) to avoid this. The packing frustration of a phase might therefore be defined as the energy penalty encompassing any deformation of the amphiphile away from its average preferred shape in that phase. The concept of packing frustration has also been applied more generically to other self-assembled systems such as block copolymers<sup>32</sup> and dendrons.<sup>33</sup> The model we will be adopting follows on from the work of Kirk, Gruner, and Stein<sup>25</sup> and also Duesing, Templer, and Seddon.<sup>21</sup> Here, the polar–apolar interface has constant mean curvature (the mean curvature being half the sum of the principal curvatures at any point) and the packing frustration energy is determined by modeling the hydrocarbon chains as Hookean springs, which have to be extended or compressed from their average length to fill the hydrophobic space. The surface averaged chain packing energy  $\langle g_p \rangle$  is therefore given by

$$\langle g_p \rangle = \lambda \frac{\int_A (\langle l \rangle - l)^2 dA}{\int_A dA} \quad (1)$$

where  $l$  is the chain length at a point projected perpendicularly away from the polar–apolar interface,  $\langle l \rangle$  is the average chain length,  $A$  is the surface area of the interface over which the variation in chain length must be integrated, and  $\lambda$  is the chain stretching modulus. In this model, therefore, the energy tied up in packing frustration is proportional to the variance in chain extension. It should be noted that this is a very simplistic model, since by maintaining a constant mean interfacial curvature and extending/compressing chains we are varying molecular density. In block copolymer systems, packing frustration has been assessed in an alternative way by modeling the variation in curvature, where a low standard deviation in the mean curvature,  $\sigma_H$ , reflects a small degree of packing frustration.<sup>32,34</sup> In this way, Matsen et al. were able to demonstrate that the gyroid phase was more stable than both the double-diamond and perforated-lamellar phases.<sup>32</sup> Preliminary experimental studies have also been performed on block copolymer systems to measure  $\sigma_H$  for the gyroid morphology; however, these were found to be significantly higher than those predicted.<sup>35</sup> More sophisticated models have been developed,<sup>36,37</sup> but the Hookean model proposed here provides

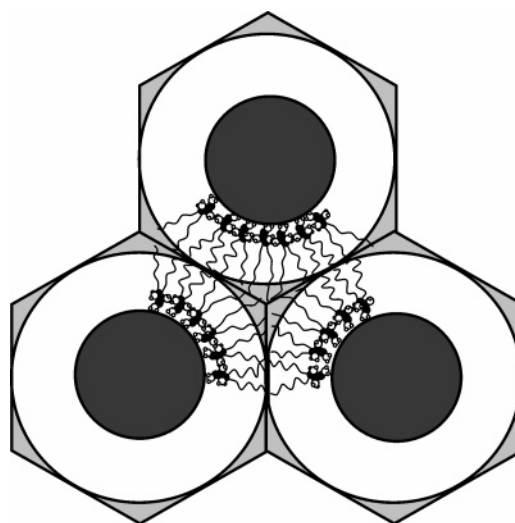


**Figure 3.** Chain packing frustration is easily visualized by sketching a cross section through the  $H_{II}$  phase. For polar–apolar interfaces with uniform circular cylindrical curvature, hydrocarbon chains must deform away from their preferred length either by extension or by compression to fill the interstitial voids represented by the light gray regions. The water channels are shaded dark gray.

us with an approachable means to gaining semiquantitative insight into the energetics driving inverse lyotropic phase behavior.

**Inverse Bicontinuous Cubics.** It is generally agreed that the surfaces defining the bilayer midplane of the inverse bicontinuous cubic phases are the triply periodic minimal surfaces (TPMS), in particular, the primitive or P surface for  $Q_{II}^P$  (crystallographic symmetry  $Im\bar{3}m$ ), the double diamond or D surface for  $Q_{II}^D$  (crystallographic symmetry  $Pn\bar{3}m$ ), and the gyroid or G surface for  $Q_{II}^G$  (crystallographic symmetry  $Ia\bar{3}d$ ). The location of the TPMS within the bilayer was confirmed experimentally by Luzzati et al.<sup>38</sup> The TPMS at the bilayer midplane have a mean curvature that is zero at every point. In other words, at any point the two principal curvatures have equal magnitude, but opposite signs; they are either saddle points or flat umbilic points. Surfaces projected away from this midplane which are parallel to it (i.e., at a constant distance from it) have a surface that either is flat (above the umbilic points) or has a net mean curvature toward the water. The constant mean curvature surfaces, which vary in distance from the midplane at different points, have the same mean curvature toward the water at all points.

To model the geometry of inverse bicontinuous phases, a monolayer must be placed on either side of the TPMS. Researchers have used the two geometries mentioned above to achieve this: a surface for the polar–apolar interface that is parallel to the TPMS or one that has constant mean curvature at the polar–apolar interface.<sup>26,39</sup> These two geometrical models of the interface impose rather different conditions on the deformation of amphiphiles in these phases. In the parallel interface model, chain extension is uniform but there is significantly greater variation in the anisotropic splay of the amphiphiles. For the constant mean curvature interface, the variation in splay is reduced, but at the cost of variations in chain extension.<sup>20</sup> An inherent consequence of the constant mean curvature surface lying at the polar–apolar interface is that the contact area between the lipids and water is minimized, therefore reducing the interfacial free energy.

(31) Sadoc, J. F.; Charvolin, J. *J. Phys. II* **1986**, *47*, 683–691.

(32) Matsen, M. W.; Bates, F. S. *Macromolecules* **1996**, *29*, 7641–7644.

(33) Ungar, G.; Liu, Y. S.; Zeng, X. B.; Percec, V.; Cho, W. D. *Science* **2003**, *299*, 1208–1211.

(34) Matsen, M. W. *J. Phys.: Condens. Matter* **2002**, *14*, R21–R47.

(35) Jinnai, H.; Nishikawa, Y.; Spontak, R. J.; Smith, S. D.; Agard, D. A.; Hashimoto, T. *Phys. Rev. Lett.* **2000**, *84*, 518.

(36) Hamm, M.; Kozlov, M. M. *Eur. Phys. J. B* **1998**, *6*, 519–528.

(37) Hamm, M.; Kozlov, M. M. *Eur. Phys. J. E* **2000**, *3*, 323–335.

(38) Luzzati, V.; Vargas, R.; Mariani, P.; Gulik, A.; Delacroix, H. *J. Mol. Biol.* **1993**, *229*, 540–551.

(39) Hyde, S. T. *J. Phys. Chem.* **1989**, *93*, 1458–1464.



It is more straightforward to calculate the geometry and energetics of a parallel interface. This has therefore been the geometry used in all reports<sup>19,22,24</sup> except for one:<sup>20</sup> that of the energetic behavior of the inverse bicontinuous cubic phases. However, it has been remarked previously<sup>21</sup> that since the measured magnitude of the Gaussian curvature modulus is smaller than the mean curvature modulus,<sup>30</sup> one would conclude that amphiphilic systems would tend toward interfaces of constant mean curvature. Ultimately, a more refined model would allow a competition between these two extreme geometries: that of constant mean curvature and constant thickness. A system in which the interfacial free energy dominated the chain stretching modulus would be expected to adopt the constant mean curvature geometry.

Constant mean curvature interfacial geometry breaks the degeneracy in local energetics which is part and parcel of the parallel interface model. This has already been shown for the curvature elastic energy<sup>20</sup> but not for the chain packing energy of eq 1.

The packing frustration of the constant mean curvature surface for  $Q_{II}^D$  as a function of hydration was first modeled by Anderson, Gruner, and Leibler,<sup>26</sup> and we follow their approach in recalculating this and extending the calculations to  $Q_{II}^P$  and  $Q_{II}^G$ . In their work, monolayer thickness is expressed as a dimensionless quantity,  $l'$ , by setting the unit cell to have sides of unit length. Equation 1 is then re-expressed in terms of the surface averages of  $l'$  and  $l'^2$

$$\langle g_p \rangle = \lambda(\langle l'^2 \rangle - \langle l' \rangle^2) a^2 \quad (2)$$

where  $a$  is the lattice parameter and  $\lambda$  is the modulus for chain extension (expressed in  $\text{N m}^{-1}$ ).

To first order approximation, Anderson, Gruner, and Leibler found that the dimensionless variance in monolayer thickness for  $Q_{II}^D$  was given by

$$\langle l'^2 \rangle - \langle l' \rangle^2 = 3.5 \times 10^{-4} \phi_l^2 + \dots \quad (3)$$

where  $\phi_l$  is the amphiphile volume fraction.

**Method of Calculation.** We used the “Surface Evolver” program<sup>40</sup> for both the generation of the constant mean curvature and underlying minimal surfaces and the calculations of the variation in bilayer thickness.<sup>41</sup> The program evolves any given surface toward its minimal surface energy, taking into account constraints and boundary conditions that have been set. Successively denser triangulations of the surface and iterations produce an improved, more accurate, energetically minimized surface. A complete description of the software can be found at <http://www.susqu.edu/brakke/evolver/html/>.

The three primitive minimal surfaces, on which the bicontinuous cubic phases are modeled, can be built up from a “fundamental patch” or a “Flächenstück” that, under the appropriate symmetry operations, can be tessellated in space to form the TPMS. The number of fundamental patches required to form an entire surface is therefore dependent on the space group of the minimal surface. Data files previously written for the P and D minimal surfaces<sup>42</sup> were modified, where the generating patch for the  $Q_{II}^P$  cubic phase was twice that of the fundamental patch. In a similar way, the generating patches for the  $Q_{II}^D$  and  $Q_{II}^G$  phases also consist of

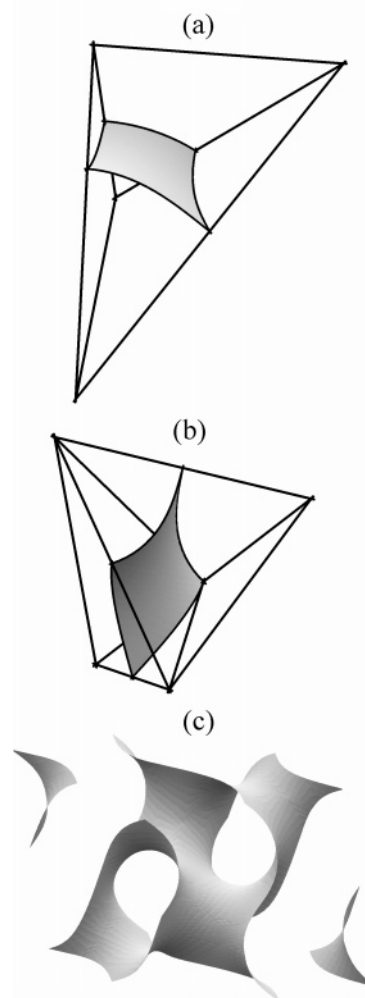


**Figure 4.** (a) Flächenstück and constraint lines for the primitive, (b) generating patch and constraint lines for the diamond, and (c) starting domain for the gyroid.

a number of fundamental patches. The reason for the differences in the number of fundamental patches in our generating patches is so that the vertices and edges of the generating patch can move during surface evolution, a necessary requirement. This can be seen directly for the P and D patches shown in Figure 4. The constraints set on the system are that the generating patch must contact the walls of the bounding boxes, divide the volumes of the boxes at the volume fraction imposed, and have uniform mean curvature. To do this, the generating patch must be able to slide up and down along the wall of the bounding box. The G surface is more complex to generate. We have adapted a data file written and generously provided by K. Große-Brauckmann in which the fundamental domain is defined within a toroidal box.<sup>43</sup> This was possible, as shown by Ross<sup>44</sup> and Große-Brauckmann,<sup>45</sup> since the gyroid divided by its translation is a minimum of area under any deformations preserving volume.

In generating our constant mean curvature surfaces, we found that as we approached the energetic minimum, it was both more accurate and efficient to use a quadratic rather than linear approximation for the energy of the perturbed surface. In practice, this means switching on the “Hessian” command<sup>40</sup> in “Surface Evolver”. It is more sensitive to extremely small perturbations than the first-order derivative but unsuitable when it is a long

(40) Brakke, K. A. *Exp. Math.* **1992**, *1*, 141–165.

(41) Motherwell, M.-L. Exact computation of the Schwarz D, Schwarz P and Schoen G minimal surfaces and their constant mean curvature families using surface evolver: a model for inverse bicontinuous cubic phases used to calculate variance in bilayer half-thickness. Imperial College London, 2001.

(42) Brakke, K. A. *Philos. Trans. R. Soc. London, Ser. A* **1996**, *354*, 2143–2157.

(43) Große-Brauckmann, K. *Exp. Math.* **1997**, *6*, 33–50.

(44) Ross, M. *Differ. Geom. Appl.* **1992**, *2*, 179–195.

(45) Große-Brauckmann, K. *Math. Z.* **1993**, *214*, 527–565.

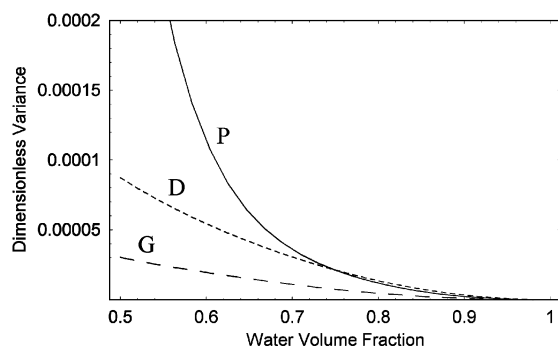


**Figure 5.** Calculated dimensionless variance in monolayer thickness for the three bicontinuous cubic phases with interfaces of constant mean curvature. The solid line, dotted line, and dashed line relate to the P, D, and G phases, respectively.

way from convergence. The interfacial area as a function of volume fraction calculated in this manner agreed within the precision of our calculations with those previously determined by Anderson and co-workers<sup>46</sup> using their own algorithms.

The average distance between the constant mean curvature patch and the minimal surface for any of the three cubics was determined by subtending normal vectors from each of the triangular facets of the minimal surface in its finite-element representation, and the intersection point was found. It should be noted that the density of triangulation over the generating patch after evolution is not constant, and therefore, to avoid bias, a weighted statistic for the average monolayer thickness over the surface of constant mean curvature was used

$$\langle l \rangle = \frac{1}{A_T} \sum_i l_i A_i \quad (4)$$

where  $A_T$  denotes the total area of the minimal surface from which the normals are dropped,  $A_i$  is the area of the  $i$ th triangular facet on the minimal surface, and  $l_i$  the length of the vector from the  $i$ th triangular facet to the bilayer midsurface. Further details of the code used for these calculations are provided in Appendix A.

**Computed Results.** We have computed the dimensionless variance in chain extension,  $\langle l'^2 \rangle - \langle l' \rangle^2$ . The results are tabulated in Appendix A and plotted in Figure 5.

For  $\phi_w < 0.75$ , the dimensionless variance is the greatest for  $Q_{II}^P$  and the least for  $Q_{II}^G$ . We can understand this behavior to some extent by noting the nature of the junctions in the bicontinuous cubic phases.  $Q_{II}^P$  has six channels meeting at a junction,  $Q_{II}^D$  has four channels, and  $Q_{II}^G$  three channels (Figure 6). As  $\phi_w$  decreases, the interface around these junctions tends more and more toward a sphere to maintain constant mean curvature. In fact, this behavior can only be sustained down to a limiting value of  $\phi_l$  before the channels are pinched off (Figure 6). This pinching off occurs at water volume fractions of 0.500, 0.262, and 0.112 for  $Q_{II}^P$ ,  $Q_{II}^D$ , and  $Q_{II}^G$ , respectively. These values and the images in Figure 6 show that it is more difficult to create a spherical interface around junctions of lower connectivity and that where the junction interface is spherical, pinching off occurs at lower values of  $\phi_w$ . Pinching off is, of course, a reflection of large scale variance in monolayer thickness, and we can get some sense of this by plotting the minimum and maximum dimensionless monolayer width as a function of  $\phi_w$  (Figure 7).

In Figure 8, we show the distribution in distances across the constant mean curvature surface for the three phases which show

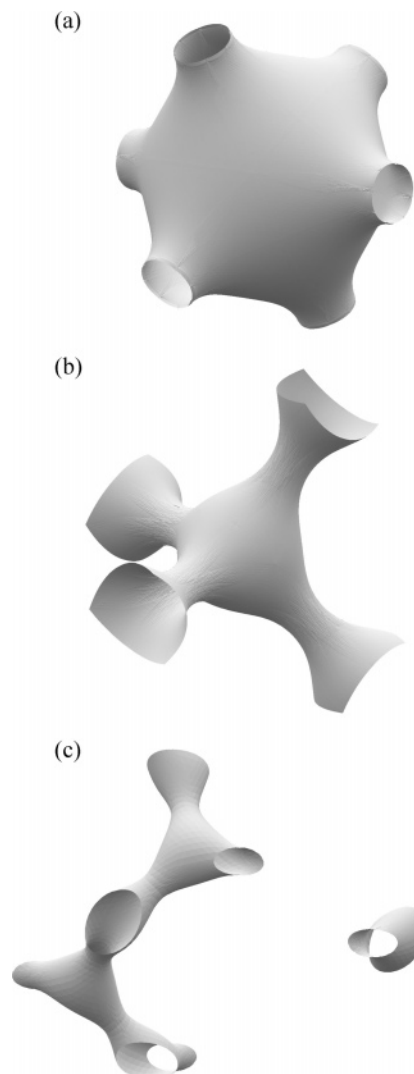


**Figure 6.** Constant mean curvature interfaces showing pinching at low water composition: (a)  $Q_{II}^P$  at  $\phi_w = 0.25$ , (b)  $Q_{II}^D$  at  $\phi_w = 0.188$ , and (c)  $Q_{II}^G$  at  $\phi_w = 0.117$ .

how packing frustration builds up around umbilic and saddle points. The saddle points sit over the regions where the channels pinch off and the umbilic points sit over the junction, showing that there is chain extension around the channels and compensatory chain compression around the junction.

This explanation for the behavior that we observe is satisfactory for  $\phi_w < 0.75$ , but there is an unexpected crossover between the dimensionless variance in the monolayer thickness of  $Q_{II}^P$  and  $Q_{II}^D$  at  $\phi_w \approx 0.75$ . As far as we have been able to determine, the observation is not an artifact of any computational imprecision in our calculations and we must therefore conclude that it is caused by a subtle geometrical effect that we are not yet able to understand.

In the limit that  $\phi_w$  tends to 1, the variance in monolayer thickness does not tend to zero. In Figure 9, we have plotted our calculations for the variance in monolayer thickness for the lipid 1-monoolein. To do this, one needs to multiply the dimensionless variance by  $a^2(\phi_l)$  and the details of this are shown in Appendix B. Once again, this result is unexpected, but it does not appear to be an artifact of the precision of our calculations.

## Experimental Section

To our knowledge, there have been no experimental measurements that reveal the packing stress within inverse bicontinuous cubic

(46) Anderson, D. M.; Davis, H. T.; Scriven, L. E.; Nitsche, J. C. C. *Adv. Chem. Phys.* **1990**, *77*, 337–396.

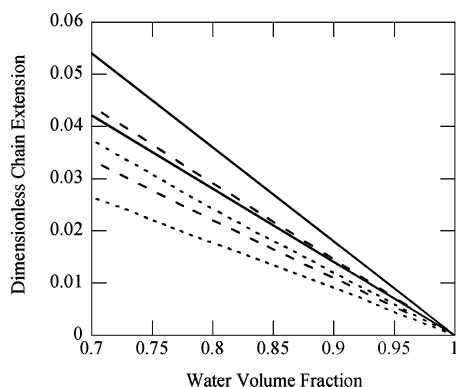


**Figure 7.** Calculated dimensionless minimum and maximum chain extension from the constant mean curvature interface to the bilayer midplane. Data for  $Q_{II}^G$  are shown as solid lines, those for  $Q_{II}^P$  are shown as dashed lines, and those for  $Q_{II}^D$  are shown as dotted lines. The calculated behavior in every case appears to be linear, and there is considerably more overlap in the region of chain extension between  $Q_{II}^P$  and  $Q_{II}^D$  than there is between  $Q_{II}^G$  and  $Q_{II}^P$ .

phases. Our model predicts that there should be differences between the different cubic phases. In particular, there are two semiquantitative predictions that the model makes. The first of these is that, in a system where the  $Q_{II}^D$  structure is the equilibrium excess water phase, the addition of a component that will release packing stress should stabilize the  $Q_{II}^P$  phase. We have done this by adding tricosane to 1-MO in excess water. The second prediction of the model is that, if one can hydrate the  $Q_{II}^D$  structure beyond its equilibrium size, one will eventually destabilize the  $Q_{II}^D$  structure in favor of  $Q_{II}^P$ . We have been fortuitous in observing this behavior during recently reported work on out-of-equilibrium structural intermediates that we find during the course of phase transitions within multilamellar vesicles of ME in excess water.<sup>29</sup>

**Materials.** The monoacylglycerides 1-MO and ME were purchased from Larodan AB (Malmö, Sweden) with a stated purity of >99% and checked using thin layer chromatography. The long-chain  $C_{23}$  alkane tricosane was obtained from Sigma Aldrich (Dorset, England) with a given purity of 99% and used as received. Triply distilled and deionized water was used throughout for the hydration of samples. High-performance liquid chromatography (HPLC) grade solvents were procured from Sigma Aldrich with a purity of >99%.

1-MO/tricosane samples at differing molar ratios were made by weighing the desired quantities of dry 1-MO and tricosane (with a precision of  $\pm 0.2$  mg) to produce a combined weight of  $\sim 200$  mg. Both 1-MO and tricosane were then dissolved in cyclohexane, mixed, dried down to a concentrated solution using  $N_2$  gas, and then introduced into a 1.5 mm diameter glass X-ray capillary (W. Müller, Berlin, Germany). The sample was lyophilized to produce a dry powder and then weighed before adding twice the weight of water. This ensured that the sample corresponded to an excess water mixture. Finally, the X-ray capillary was flame-sealed, heated above the melting point of tricosane ( $47.6^\circ\text{C}$ ),<sup>47</sup> centrifuged up and down the capillary, and then thermally cycled between  $-25$  and  $60^\circ\text{C}$  to ensure thorough and uniform mixing. All samples were stored at  $4^\circ\text{C}$  and used within a week of preparation.

ME samples were made in glass vials by adding at least 90 wt % water to the lipid. Homogenization was achieved by subjecting the resulting mixture to at least 30 thermal cycles between  $-20$  and  $60^\circ\text{C}$ . This resulted in samples composed of multilamellar (or onion) vesicles with a narrow size distribution (cryo-TEM measurements gave an average diameter  $\approx 200 \pm 20$  nm). These vesicular domains were stable over a period of at least 1 day when stored at  $4^\circ\text{C}$ , and measurements were made within this period. The measurements made of the structural transformations that occur in this system in

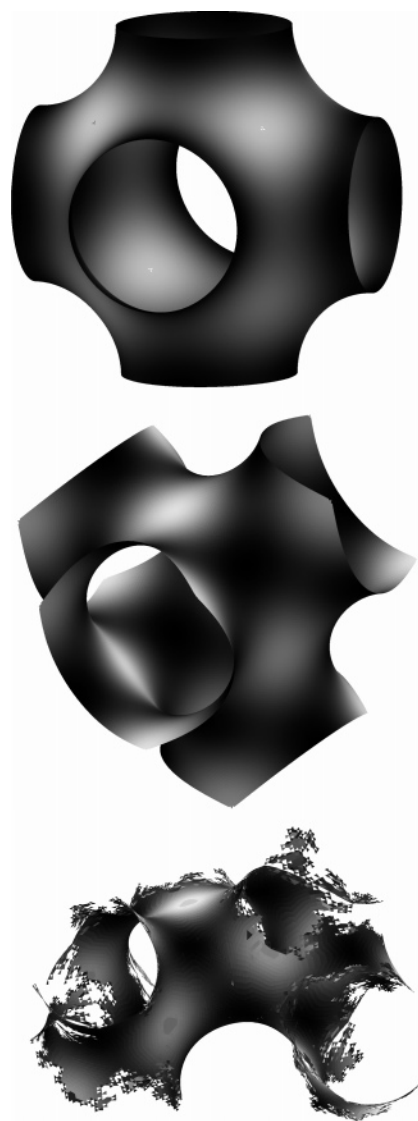


**Figure 8.** Surface contour plot of the distribution of chain extension and compression between the constant mean curvature interface and the bilayer midplane for (a) the P phase, (b) the D phase, and (c) the G phase. Black indicates chain extension, and white indicates compression.

the transit from the lamellar to the  $Q_{II}^D$  phase were made using hydrostatic pressure jumps. Freshly cycled samples were thus housed in a custom built high-pressure X-ray sample cell with flat diamond windows, whose design has been described previously,<sup>48</sup> with the sample being held in a Teflon aperture between two Mylar windows.

**X-ray Measurements.** Small-angle X-ray diffraction measurements on the 1-MO/tricosane system were used for definitive phase determination and to obtain lattice parameters for all samples. Phase identifications were further confirmed by polarizing microscopy and examination of the birefringent textures in each phase.

The X-ray source was a GX-20 rotating anode generator (Nonius, Netherlands) Ni-filtered for Cu K $\alpha$  radiation ( $\lambda = 1.54 \text{ \AA}$ ). Double-mirror Franks optics were used to focus the radiation to a  $190 \mu\text{m}$  point. Parasitic scatter was minimized by evacuation of all beamline components. The temperature of the sample was servo-controlled to a precision of  $\pm 0.03^\circ\text{C}$  using Peltier elements via a microcontroller interface linked to a computer. The sample temperature and all other elements involved in the X-ray experiments, such as shutter control and data analysis, were managed using the TV4 software package developed by E. F. Eikenberry (Paul Scherrer Institute/Swiss Light

(47) Small, D. M. The Physical Chemistry of Lipids, From Alkanes to Phospholipids. In *Handbook of Lipid Research*; Hanahan, D. J., Ed.; Plenum Press: New York, 1986; Vol. 4.

(48) Erbes, J.; Winter, R.; Rapp, G. *Ber. Bunsen-Ges. Phys. Chem.* **1996**, *100*, 1713–1722.



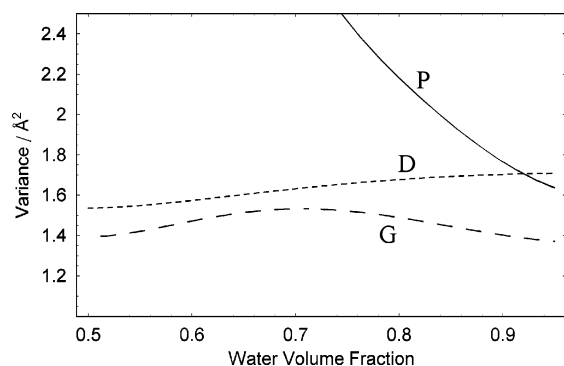


**Figure 9.** Calculated variance in chain extension of the three bicontinuous cubic phases for the 1-MO system. The following values were used for the calculations for the molecular geometry of 1-MO (see Appendix B for details):  $v_n = 465 \text{ Å}^3$ ,  $A_n = 33 \text{ Å}^2$ , and  $v = 612 \text{ Å}^3$ . The solid line, dotted line, and dashed line relate to the P, D, and G phases, respectively.

Source, Switzerland) and S. M. Gruner (Cornell University, New York) and modified by ourselves.<sup>49</sup> The X-ray spacings were calibrated against silver behenate ( $d = 58.4 \text{ Å}$ ).

For the kinetic measurements on ME, pressure-jump experiments were carried out at the ID02 beamline of the European Synchrotron Radiation Facility (ESRF), Grenoble (France) using a high-pressure X-ray sample cell capable of altering hydrostatic pressure within 7 ms.<sup>50</sup>

Experiments were carried out at a wavelength of  $0.7514 \text{ Å}$  with beam dimensions of  $200 \mu\text{m}$  by  $400 \mu\text{m}$  in the vertical and horizontal directions, respectively. Measurements were calibrated against silver behenate and rat-tail collagen. This high energy beam maximizes transmission through the diamond windows which surround the sample in the high-pressure cell. Two-dimensional diffraction images were recorded on an image-intensified charge-coupled device (CCD) detector consisting of an X-ray image intensifier (Thomson TTE) coupled to a FreLoN (fast-readout low-noise) CCD device developed at the ESRF. The CCD has a frame rate of just under 10 frames per second ( $1024 \times 1024$  pixels).

Pressure jumps were made using an apparatus designed and built at the University of Dortmund. The apparatus can perform bidirectional pressure jumps of variable amplitude in a time of less than 7 ms. Elevated hydrostatic pressures of between 0.1 and 4 kbar (with a precision of  $\pm 10$  bar) were achieved by means of a manual pump acting on a reservoir of water. Temperature control (with a precision of  $\pm 0.2 \text{ °C}$ ) was via a system of circulating water from a thermostat through the temperature control jacket of the cell. A detailed description of the apparatus is provided elsewhere.<sup>51</sup>

## Results and Discussion

**Release of Chain Packing Stress.** Before heating, the 1-MO/tricosane/excess water samples were all cooled to  $-15 \text{ °C}$ , which induced the lamellar gel or  $L_\beta$  phase. This meant that all samples were observed from a common baseline. Each sample was then heated to  $50 \text{ °C}$ , and above  $15 \text{ °C}$ , measurements were taken at  $1 \text{ °C}$  intervals with a 15 min pause for sample equilibration at each temperature. The phase behavior as a function of temperature was determined for a range of alkane mole fractions in the interval,  $0.02 \leq x_A \leq 0.35$ , where  $x_A$  is given by

$$x_A = \frac{n_A}{n_A + n_L} \quad (5)$$

and  $n_A$  and  $n_L$  are the moles of tricosane and 1-MO in the mixture, respectively. The phase behavior at a number of values of  $x_A$  is shown in Figure 10. Extremely low tricosane concentrations exhibit similar phase behavior to that of the binary 1-MO/excess water system at all temperatures studied (see Figure 2 for comparison). However, at  $x_A = 0.04$ , the  $H_{II}$  phase is induced at  $41 \text{ °C}$  (we show the data for  $x_A = 0.06$ ). No significant change in the phase behavior is then seen until  $x_A = 0.10$ , at which point the  $Q_{II}^P$  phase ( $Im3m$  symmetry) is observed between the  $L_\beta$  and  $Q_{II}^D$  phases, first making its appearance at  $\sim 18 \text{ °C}$ . At higher tricosane mole fractions between  $0.25 \leq x_A \leq 0.27$ , the inverse micellar cubic,  $Q_{II}^m$ , phase with  $Fd3m$  symmetry makes its appearance. This is replaced by the inverse micellar,  $L_2$ , phase at higher tricosane concentrations.

The addition of a long-chain alkane is known to lower the packing frustration of a lyotropic liquid-crystalline system by partitioning into the regions otherwise filled by amphiphilic hydrocarbon chains that have had to deform.<sup>21,23,25,52</sup> If the chain packing frustration of a system is reduced, the desire to attain a uniform and two-dimensionally isotropic interfacial curvature will dominate.<sup>30</sup>

Without relief of the packing frustration, only the  $Q_{II}^D$  phase is stable above  $18 \text{ °C}$ . However, a low tricosane mole fraction will stabilize the  $Q_{II}^P$  phase in preference to  $Q_{II}^D$  at this temperature. We can understand this result from calculations of the packing stress and curvature elastic energy of a constant mean curvature interface. The computed packing stress in  $Q_{II}^P$  is much greater than it is for  $Q_{II}^D$  (Figure 9). However, in this model, the curvature elastic energy of  $Q_{II}^P$  is less than that of  $Q_{II}^D$ . Adding tricosane has allowed the system to reduce the system's overall free energy by reducing the packing stress in  $Q_{II}^P$ . This then destabilizes  $Q_{II}^D$ , which in the absence of any chain packing stress is always the more energetically costly phase with respect to  $Q_{II}^P$ .

It should be remembered that the behavior reported here all occurs below the normal melting point of tricosane. This indicates that the magnitude of the packing energy in  $Q_{II}^P$  is significant and is further evidence to support the hypothesis that it is the differences in the packing and curvature elastic energies among the inverse bicontinuous cubics that governs their phase behavior.

Although this report focuses on the packing stress in the inverse bicontinuous cubic phases, the behavior of the other observed inverse phases is also informative. The phase sequence recorded from Figure 10d onward shows a clear sequence from bicontinuous cubic to  $H_{II}$ ,  $Q_{II}^m$ , and  $L_2$ . This is entirely consistent with the increasing volume of tricosane that is needed to pack into the stressed regions of these phases.<sup>21</sup> The appearance of the  $H_{II}$  phase at lower volume mole fractions of tricosane than  $Q_{II}^P$  confirms previous measurements that indicated that the chain packing energy in the  $H_{II}$  phase was significantly greater than that in the bicontinuous cubic phases.<sup>20</sup>

**Swollen Bicontinuous Cubic Structures.** Our results on highly swollen cubic structures were a serendipitous byproduct of research being carried out on the structural dynamics of the  $L_\alpha$  to  $Q_{II}^D$  phase transition.<sup>29</sup> In preparing the ME samples, by the methods described above, we observed that highly swollen metastable inverse bicontinuous cubic phases were formed in coexistence with the  $L_\alpha$  phase (Figure 11). The evidence reported by us<sup>29</sup> indicates that these swollen cubic phases are located in the core of the onion vesicles<sup>53</sup> formed by the sample processing method used. It has been hypothesized that the bicontinuous

(49) Seddon, J. M.; Templer, R. H.; Warrender, N. A.; Huang, Z.; Cevc, G.; Marsh, D. *Biochim. Biophys. Acta* **1997**, *1327*, 131–147.

(50) Squires, A. M.; Templer, R. H.; Seddon, J. M.; Woenckhaus, J.; Winter, R.; Narayanan, T.; Finet, S. *Phys. Rev. E* **2005**, *72*.

(51) Woenckhaus, J.; Kohling, R.; Winter, R.; Thiagarajan, P.; Finet, S. *Rev. Sci. Instrum.* **2000**, *71*, 3895–3899.

(52) Rand, R. P.; Fuller, N. L.; Gruner, S. M.; Parsegian, V. A. *Biochemistry* **1990**, *29*, 76–87.

(53) Diat, O.; Roux, D.; Nallet, F. *J. Phys. II* **1993**, *3*, 1427–1452.



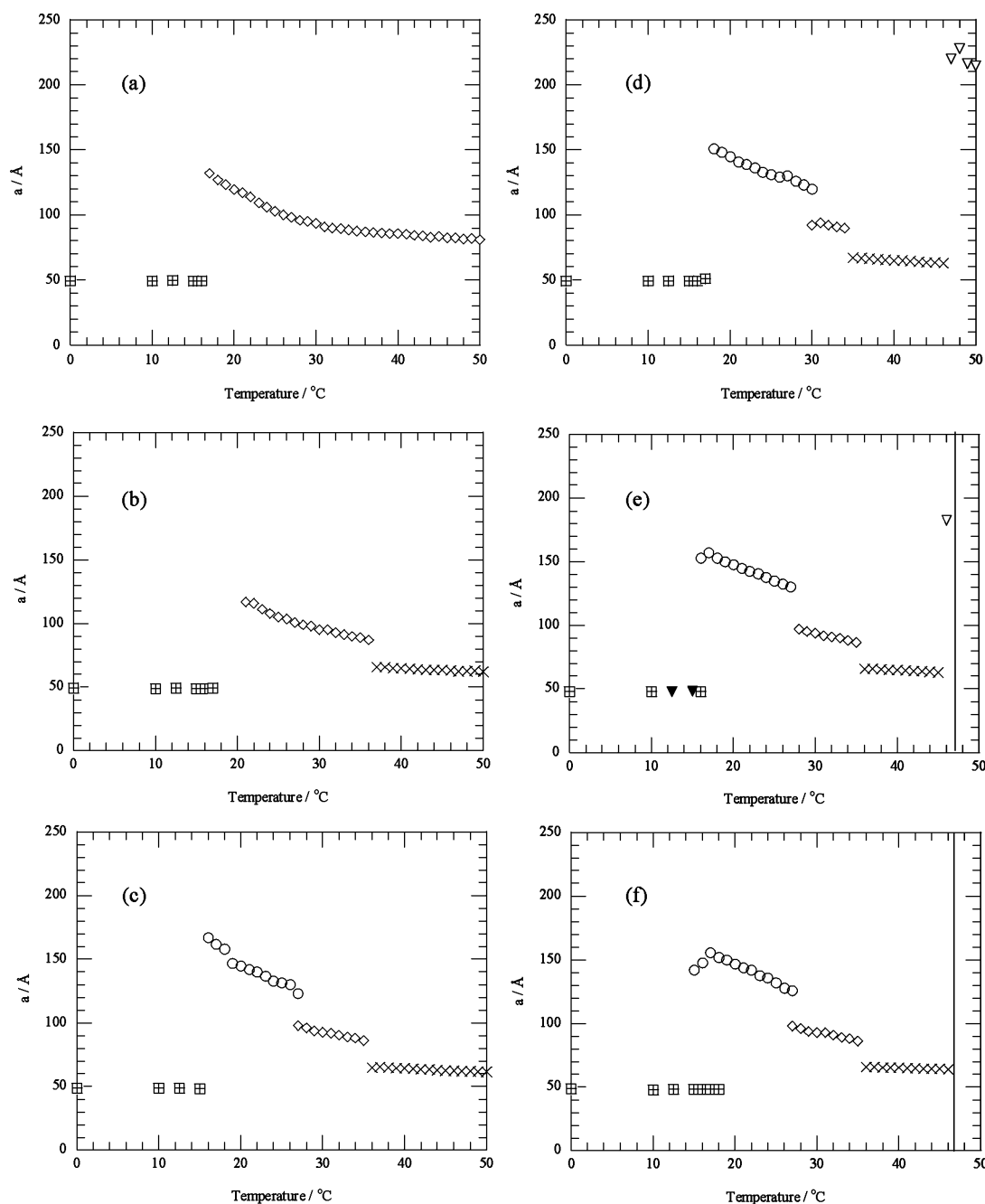


**Figure 10.** Phase and structural behavior of 1-MO/tricosane mixtures in excess water. Phase and lattice parameters are recorded as a function of temperature for tricosane compositions of (a)  $x_A = 0.02$ , (b)  $x_A = 0.06$ , (c)  $x_A = 0.10$ , (d)  $x_A = 0.25$ , (e)  $x_A = 0.27$ , and (f)  $x_A = 0.35$ . The inverse micellar,  $L_2$ , phase exists at high temperatures denoted by the region to the right of the vertical line in the phase diagrams of both (e) and (f). The phases are denoted by the differing data point markers, that is, square grid,  $L_\alpha$ ; tilted cross,  $H_{II}$ ; tilted square,  $Pn3m$ ; circle,  $Im3m$ ; empty triangle,  $Fd3m$ ; filled triangle,  $L_\alpha + \text{nascent } Im3m$ .

cubic phase is stretched under an isotropic tension exerted by the multilamellar vesicle in which it is encased. Although these swollen structures are metastable, they persist for the order of 1 day.

The first pertinent observation made on these swollen structures is that we observe both  $Q_{II}^D$  and  $Q_{II'}^D$ , with the former being found in coexistence with the  $L_\alpha$  phase and the latter being found in coexistence with the  $L_\beta$  phase. For the swollen  $Q_{II}^D$  structure, we find that there is a very distinct maximum lattice parameter of  $220 \pm 0.4$  Å. The structure disappears upon increasing the hydrostatic pressure or decreasing the temperature, both of which act so as to swell the inverse bicontinuous structures. Interestingly, we also observe a swollen  $Q_{II}^D$  structure as an intermediate during the  $L_\alpha$  to  $Q_{II}^D$  phase transition and here we

also observe a maximum lattice parameter of  $220 \pm 0.4$  Å. These results indicate that there is an absolute stability limit to forming the  $Q_{II}^D$  structure at this size. Using the expressions relating lattice parameter and water volume fraction in Appendix B, we can estimate the equivalent water composition by approximating the lipid geometry of ME to that of 1-MO. This should be a good approximation, and it estimates the maximum water composition in the  $Q_{II}^D$  structure to be  $\phi_w = 0.74$ .

If we continue to increase hydrostatic pressure beyond the limit where  $Q_{II}^D$  disappears, the enveloping lamellar vesicle undergoes a chain freezing transition into the  $L_\beta$  phase. The lamellar gel phase has a lower water content than the fluid lamellar phase, and as a consequence, water must be expelled from between the multilamellar stacks. Since we can cycle back down in pressure

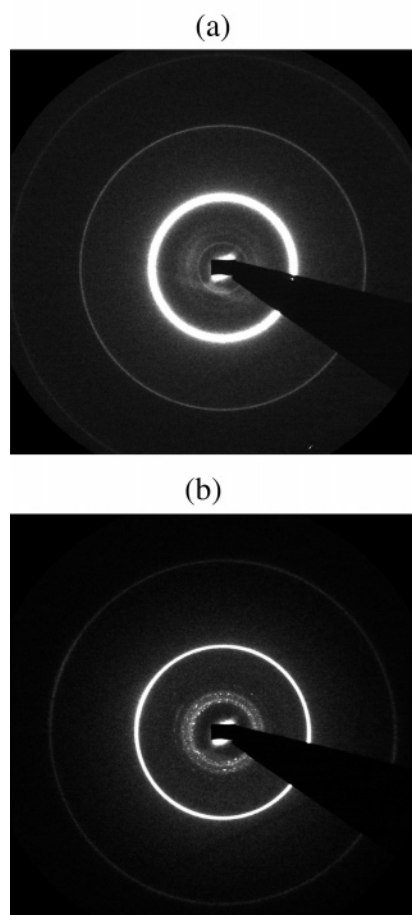


**Figure 11.** Two-dimensional diffraction patterns of highly swollen inverse bicontinuous structures obtained for the lipid system ME in excess water using the ID02 High Brilliance beamline at the ESRF: (a)  $Q_{II}^P$  structure ( $a = 309$  Å) coexisting with lamellar gel phase and (b) swollen  $Q_{II}^D$  structure ( $a = 220$  Å) coexisting with the fluid lamellar phase.

and return to precisely the same structure and geometry, we conclude that the water is expelled into the core of the onion vesicle, into the region occupied by the swollen cubic structure. Concomitant with the appearance of the  $L_\beta$  phase, we observe the appearance of a swollen  $Q_{II}^P$  structure with a lattice parameter of  $310 \pm 4$  Å, which equates to a water composition in the structure of  $\phi_w = 0.76$ .

We have attempted, with partial success, to record the moment of transition. In Figure 12, we show the integrated scattering intensity pattern for a sample taken through a pressure decrease from 1.5 to 1.3 kbar at 46.6 °C. This jump takes the system from a  $Q_{II}^P$  structure with a lattice parameter of 307 Å to the  $Q_{II}^D$  structure. In making this transition, we lose definition in the Bragg peaks of these structures, with a broadening of the disappearing and emerging first-order peaks. Measurement of the lattice parameters from these two peaks gives us estimates of the lattice parameters of  $Q_{II}^P$  and  $Q_{II}^D$  (313 and 216 Å, respectively) which are entirely consistent with the more precise static measurements.

We believe that the most straightforward interpretation of the behavior we have reported above is that at a water composition of approximately  $\phi_w = 0.75$  the total free energies of the  $Q_{II}^P$  and  $Q_{II}^D$  structures are equal. The constant mean curvature interfacial geometry predicts precisely such a transition as a result of the decreasing difference in the chain packing free energy of these structures as they become swollen.

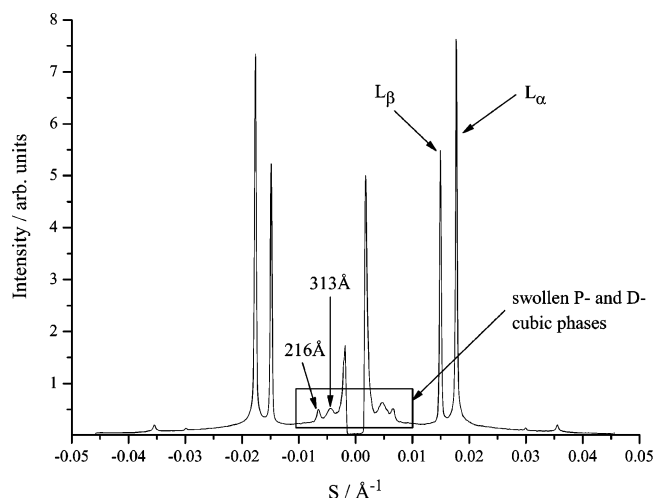


**Figure 12.** Plot of X-ray intensity with respect to the scattering angle recorded during the transition from a highly swollen  $Q_{II}^P$  structure to a highly swollen  $Q_{II}^D$  structure. The first-order peaks from the fluid and gel lamellar phases can be seen in coexistence, and the broadened first-order peaks of the  $Q_{II}^P$  and  $Q_{II}^D$  structures appear at lower angles. The visible streaks are caused by the diamond windows of the pressure cell used here.

## Conclusions

We have calculated that there are absolute and functional differences in the packing stress of inverse bicontinuous cubic phases modeled with interfaces of constant mean curvature. We have been able to probe the predictions of this model in two ways. In the first, we have shown that when packing stress is reduced in the  $Q_{II}^D$  phase by addition of a long-chain alkane, the  $Q_{II}^P$  phase is stabilized, consistent with the model. In the second, we have shown that when highly swollen  $Q_{II}^D$  structures are further hydrated, the  $Q_{II}^P$  structure is stabilized and this too is predicted by the model.

Our results indicate that using a constant mean curvature model for the interfacial geometry of the inverse bicontinuous cubic phases may constitute a reasonable starting point for modeling the energetics and explaining the phase behavior of these complex structures. Combining the packing energy and curvature elastic energy in the constant mean curvature model appears to provide an explanation for the experimentally determined phase behavior among the inverse bicontinuous cubic phases, and this will be the subject of a future article.

**Acknowledgment.** We wish to acknowledge the support of the Engineering and Physical Sciences Research Council of the U.K. who supported this work via a Ph.D. Studentship to B.J.K. and C.C. and a PDRA to G.S. via the Platform Grant GR/S77721/01. R.H.T. and K.B. were visitors of the Isaac Newton Institute at Cambridge University which enabled much of the computational work reported here, and M.-L.M. was in receipt of a Nuffield Foundation Studentship. We also wish to thank Dr. Karsten Große-Brauckmann for his help in setting up the calculations of the G cubic. We were aided in our collection of data from the beamline ID02 at the European Synchrotron Radiation Facility by Dr. Stephanie Finet using a high-pressure system provided by Prof. Roland Winter of Dortmund University.

## Appendix A

The variance at varying water volume fractions for each of the three cubic phases was calculated using the Surface Evolver executable file, downloadable from <http://www.susqu.edu/brakke/evolver/>. The relevant .fe data file (all .fe files used are given in the Supporting Information) for the desired cubic phase can then be loaded into Surface Evolver.

**Table A1. Calculated Variances for the P, D, and G Surfaces at Differing Water Volume Fractions**

	$Q_{II}^P$	$Q_{II}^D$	$Q_{II}^G$
1	0	0	0
0.98	$9.35448 \times 10^{-8}$	$1.36372 \times 10^{-7}$	$4.0954 \times 10^{-8}$
0.96	$3.75446 \times 10^{-7}$	$5.44667 \times 10^{-7}$	$1.691 \times 10^{-7}$
0.94	$8.53576 \times 10^{-7}$	$1.22388 \times 10^{-6}$	$3.8062 \times 10^{-7}$
0.92	$1.53941 \times 10^{-6}$	$2.17277 \times 10^{-6}$	$6.872 \times 10^{-7}$
0.9	$2.45634 \times 10^{-6}$	$3.39527 \times 10^{-6}$	$1.0855 \times 10^{-6}$
0.88	$3.62657 \times 10^{-6}$	$4.87891 \times 10^{-6}$	$1.676 \times 10^{-6}$
0.86	$5.08564 \times 10^{-6}$	$6.64644 \times 10^{-6}$	$2.1696 \times 10^{-6}$
0.84	$6.87717 \times 10^{-6}$	$8.65749 \times 10^{-6}$	$3.013 \times 10^{-6}$
0.82	$9.05737 \times 10^{-6}$	$1.09919 \times 10^{-5}$	$3.6672 \times 10^{-6}$
0.8	$1.16946 \times 10^{-5}$	$1.35262 \times 10^{-5}$	$4.746 \times 10^{-6}$
0.78	$1.48843 \times 10^{-5}$	$1.64193 \times 10^{-5}$	$5.5887 \times 10^{-6}$
0.76	$1.88162 \times 10^{-5}$	$1.94653 \times 10^{-5}$	$6.9685 \times 10^{-6}$
0.74	$2.34128 \times 10^{-5}$	$2.29172 \times 10^{-5}$	$7.9848 \times 10^{-6}$
0.72	$2.91062 \times 10^{-5}$	$2.64738 \times 10^{-5}$	$9.421 \times 10^{-6}$
0.7	$3.60737 \times 10^{-5}$	$3.04871 \times 10^{-5}$	$1.0839 \times 10^{-5}$
0.68	$4.46785 \times 10^{-5}$	$3.45861 \times 10^{-5}$	$1.251 \times 10^{-5}$
0.66	$5.53966 \times 10^{-5}$	$3.90589 \times 10^{-5}$	$1.4202 \times 10^{-5}$
0.64	$6.89035 \times 10^{-5}$	$4.38374 \times 10^{-5}$	$1.624 \times 10^{-5}$
0.62	$8.61827 \times 10^{-5}$	$4.89229 \times 10^{-5}$	$1.7563 \times 10^{-5}$
0.6	$1.16174 \times 10^{-4}$	$5.43382 \times 10^{-5}$	$1.947 \times 10^{-5}$
0.58	$1.47255 \times 10^{-4}$	$6.00839 \times 10^{-5}$	$2.1173 \times 10^{-5}$
0.56	$1.9027 \times 10^{-4}$	$6.62322 \times 10^{-5}$	$2.345 \times 10^{-5}$
0.54	$2.53669 \times 10^{-4}$	$7.28172 \times 10^{-5}$	$2.5194 \times 10^{-5}$
0.52	$3.57945 \times 10^{-4}$	$7.99289 \times 10^{-5}$	$2.778 \times 10^{-5}$
0.5	$5.76058 \times 10^{-4}$	$8.75779 \times 10^{-5}$	

Before evolving the surfaces toward their minimum energy, the desired water volume fraction can be altered by changing the volume of body [1] in the data files for the P and D phases or body [3] for the G phase, defined in the “bodies” section of the pertinent data file. The water volume fraction is a simple multiple of the body volume, specifically, 12, 2, and  $1/128$  for the P, D, and G surfaces, respectively.

Once one of the data files is loaded into Surface Evolver, the command “run” will initiate the surface refinement and calculation of the variance.

For each of our calculations, the triangulation of the P and D patches was refined six times in each case, resulting in 1024 facets per patch (49 152 per unit cell), where, after each refinement, the surface was evolved iteratively toward its minimum energy. For the G surface, this level of accuracy was not achievable, since the initial generating patch represented a much larger surface area, and was already heavily triangulated. Such refinement would therefore require both considerable computing power and time; therefore, the G surface was refined only three times, producing a surface with 24 576 facets.

For each phase, we varied the volume fraction between the minimal surface and the constant mean curvature surface systematically and obtained both the average monolayer thickness and the average of the squared monolayer thickness at each volume fraction. It should be noted that the volume fraction between the minimal surface and the constant mean curvature surface is that of a monolayer, whereas we are investigating inverse bicontinuous cubic phases that consist of bilayers.

Important considerations in each case were the dimensions of the whole unit cell, built up from the generating patch. The

calculated lengths and a resulting variance from each patch were therefore scaled to be consistent with a cubic unit cell of side length 1. For the D and P surfaces, the division factor was 4, whereas for the G surface, it was 64 due to the unit cell created in Evolver having the dimensions  $8 \times 8 \times 8$  rather than  $2 \times 2 \times 2$ .

The calculated variances for the P, D, and G surfaces at varying water volume fractions are given in Table A1.

## Appendix B

The dimensionless variance has been calculated for the three inverse bicontinuous cubic phases for a number of different water volume fractions. To facilitate the use of our data for further calculations, we have fitted them in each case as an even power series with respect to the water volume fraction and obtained values for the coefficients of the first four terms,  $\psi_1$ ,  $\psi_2$ ,  $\psi_3$ , and  $\psi_4$ :

$$R = \psi_1(1 - \phi_w)^2 + \psi_2(1 - \phi_w)^4 + \psi_3(1 - \phi_w)^6 + \psi_4(1 - \phi_w)^8 + \dots \quad (B1)$$

The first coefficient shown in Table B1 for the  $Q_{II}^D$  surface is close to the value obtained by Anderson.<sup>26</sup>

To increase the region in which the fit is accurate within a small error margin, the number of terms could be increased. For this to have relevance to experimental systems, the variation of the lattice parameter,  $a$ , with water volume fraction,  $\phi_w$ , for the system of interest must be known; see eq 2 in the main text. The lattice parameter was obtained by combining two expressions (eqs B2 and B3) for the surface area at the pivotal surface for one monolayer within the unit cell,  $S_n$ , derived by Templer et al.<sup>20</sup> for constant mean curvature interfaces

$$S_n = a^2 \sum_{i=0}^2 \sigma_i \phi_n^{2i} \quad (B2)$$

$$S_n = \frac{A_n a^3 (1 - \phi_w)}{2\nu} \quad (B3)$$

where the coefficients,  $\sigma_i$ , have been previously obtained<sup>20</sup> and the volume fraction of the pivotal surface,  $\phi_n$ , is proportional to the ratio between the pivotal surface volume,  $\nu_n$ , and the molecular volume,  $\nu$ , and can therefore be described by  $\phi_n = \nu_n / \nu (1 - \phi_w)$ . The molecular area at the pivotal surface,  $A_n$ , together with the pivotal surface volume and the molecular volume are unique for each system, and they must be experimentally determined. For 1-monoolein, these are given as  $A_n = 33 \text{ \AA}^2$ ,  $\nu_n = 465 \text{ \AA}^3$ , and  $\nu = 612 \text{ \AA}^3$ .

Finally, the lattice parameter for any given water volume fraction is given by

$$a = \left( \frac{2\nu}{A_n(1 - \phi_w)} \right) \sum_{i=0}^2 \sigma_i \phi_n^{2i} \quad (B4)$$

**Supporting Information Available:** Surface Evolver data for the P, D, and G minimal surfaces. This material is available free of charge via the Internet at <http://pubs.acs.org>.

LA700355A

**Table B1. Coefficients to Calculate the Variance in Monolayer Thickness of the Constant Mean Curvature Inverse Bicontinuous Cubics**

	$Q_{II}^P$	$Q_{II}^D$	$Q_{II}^G$
$\psi_1$	$2.10286 \times 10^{-4} \pm 1.63 \times 10^{-5}$	$3.37618 \times 10^{-4} \pm 3.25 \times 10^{-6}$	$1.03399 \times 10^{-4} \pm 2.47 \times 10^{-6}$
$\psi_2$	$2.58955 \times 10^{-3} \pm 4.41 \times 10^{-4}$	$3.37858 \times 10^{-5} \pm 5.11 \times 10^{-5}$	$4.0106 \times 10^{-4} \pm 6.05 \times 10^{-5}$
$\psi_3$	$-1.66996 \times 10^{-2} \pm 3.65 \times 10^{-3}$	$-4.89167 \times 10^{-4} \pm 2.46 \times 10^{-4}$	$-2.64235 \times 10^{-3} \pm 4.53 \times 10^{-4}$
$\psi_4$	$0.125123 \pm 9.36 \times 10^{-3}$	$2.16436 \times 10^{-3} \pm 3.66 \times 10^{-4}$	$5.28353 \times 10^{-3} \pm 1.05 \times 10^{-3}$
usable range	$0.500 < \phi_w < 1$	$0.262 < \phi_w < 1$	$0.112 < \phi_w < 1$